PNAS NEXUS

PNAS Nexus, 2025, 4, pgaf024

https://doi.org/10.1093/pnasnexus/pgaf024
Advance access publication 24 January 2025
Research Report

Loss of PRICKLE1 leads to abnormal endometrial epithelial architecture, decreased embryo implantation, and reduced fertility in mice

Emily R. Roberts [a], Aishwarya V. Bhurke [b,c], Sornakala Ganeshkumar [a], Sumedha Gunewardena [a,d], Ripla Arora [b,c] and Vargheese M. Chennathukuzhi [a,*]

[a]Department of Cell Biology and Physiology, University of Kansas Medical Center, Kansas City, KS 66160, USA
[b]Department of Obstetrics, Gynecology, and Reproductive Biology, Michigan State University, Grand Rapids, MI 49503, USA
[c]Institute for Quantitative Health Science and Engineering, Michigan State University, East Lansing, MI 48824, USA
[d]Department of Biostatistics, University of Kansas Medical Center, Kansas City, KS 66160, USA
*To whom correspondence should be addressed: Vargheese M. Chennathukuzhi. Email: vchennathukuzhi@kumc.edu
Edited By JoAnn Trejo

Abstract

Successful embryo implantation requires coordinated changes in the uterine luminal epithelium, including structural adaptations, apical–basal polarity shifts, intrauterine fluid resorption, and cellular communication. Planar cell polarity proteins, essential for cell organization, are understudied in the context of uterine physiology and implantation. PRICKLE proteins, components of PCP, are suggested to play critical roles in epithelial polarization and tissue morphogenesis. However, their function in the polarized unicellular layer of endometrial epithelium, which supports embryo implantation, is unknown. We developed an endometrial epithelial-specific knockout of mouse *Prickle1* using *Lactoferrin-iCre* to investigate its role in uterine physiology. *Prickle1* ablation in the endometrial epithelium of mice resulted in decreased embryo implantation by gestational day 4.5, leading to lower fertility. 3D imaging of the uterus revealed abnormal luminal folding, impaired luminal closure, and altered glandular length in mutant uteri. Additionally, we observed decreased aquaporin-2 expression, disrupted cellular architecture, and altered E-cadherin expression and localization in the mutant uterine epithelium. Evidence of epithelial–mesenchymal transition was found within luminal epithelial cells, further linking PRICKLE1 loss to uterine pathologies. Furthermore, altered polarity of cell division leading to incomplete cytokinesis and increase in binuclear or multinucleated cells suggests a crucial role for PRICKLE1 in the maintenance of epithelial architecture. Our findings highlight PRICKLE1's critical role in the planar cell polarity pathway within the uterus, revealing its importance in the molecular and cellular responses essential for successful pregnancy and fertility.

Keywords: Prickle1, Wnt/PCP, implantation, epithelial polarity, EMT

Significance Statement

Proper uterine luminal epithelial architecture and function are essential for embryo implantation and successful pregnancy. Cyclic changes in the shape and structure of the epithelial lining of the uterus throughout the menstrual cycle are guided by steroid hormones, estrogen and progesterone, as well as local spatial cues. Wnt/planar cell polarity (Wnt/PCP) signaling is hypothesized to provide the spatial cues to organize unicellular, 2D sheet of epithelium in a plane orthogonal to the apical–basal polarity. Conditional ablation of *Prickle1*, a crucial Wnt/PCP gene, in mouse uterine epithelium results in aberrant plane of cell division, leading to binucleated/multinucleated cells, epithelial–mesenchymal transition, and defective implantation. Our results indicate an essential role for PRICKLE1 in epithelial architecture and fertility.

Introduction

The uterine luminal epithelium is the primary maternal contact for the implanting embryo, and several steps must coincide for successful embryo implantation to occur (1). These steps include precise timing of luminal epithelial structural changes (2, 3), appropriate alterations to apical–basal polarity (4, 5), intrauterine fluid resorption (6), and cellular communication between endometrial and uterine immune cells (7, 8). However, how the uterus transiently transforms into this receptive state for proper embryo implantation is poorly understood.

The luminal epithelium must undergo several morphological changes to prepare for an implanting embryo, and this term has been previously coined plasma membrane transformation (5). During this process, the timing of this transition and the

Competing Interest: The authors declare no competing interests.
Received: August 20, 2024. **Accepted:** January 14, 2025

associated alteration to the cell structure is crucial to its success (4, 9–11). Major components of this process are specifically associated with planar cell polarity (PCP), a crucial component for proper epithelial layer formation and epithelial cell division in a specified plane of tissue (12). Some studies have investigated the chronology of these events utilizing the defective implantation of *Wnt5a* mutant mice (13). Moreover, recent work in uterine deletion of Van-Gogh-like 2 (*Vangl2*) has shown the importance of PCP and associated proteins in embryo implantation chamber formation and successful implantation in mice (14). However, the role of PCP signaling in the uterine epithelial morphogenesis and its function during implantation is still widely not understood.

PCP proteins, first identified in drosophila (15–18), provide vectorial information for cell organization and migration across a wide field. However, of the six main PCP proteins, PRICKLE has been largely understudied and particularly unstudied in PCP within the context of uterine physiology and the process of embryo implantation. The mouse genome contains four *Prickle* homologs, where *Prickle1* and *Prickle2* are the most closely related to drosophila *Prickle* gene. While the role of PRICKLE1 and PRICKLE2 has been previously studied in embryonic AB polarity (19, 20), the early embryonic lethality of their conventional knockouts has limited our knowledge of their role in late-stage tissue development (21, 22). PRICKLE1 exerts multifaceted roles in cellular polarization and tissue morphogenesis and has been implicated in regulating the noncanonical Wnt/PCP pathway (23). PRICKLE1 has yet to be studied in the context of the endometrial epithelium and its role in PCP maintenance within the uterus.

To explore the PCP-related function of PRICKLE1 in uterine physiology and embryo implantation, we developed an endometrial epithelial conditional knockout (cKO) of *Prickle1* using a *Lactoferrin-iCre*. Our results demonstrate that the loss of PRICKLE1 in the endometrial epithelium leads to decreased fertility and embryo implantation defect as early as gestational day (GD) 4.5. In addition, 3D imaging demonstrates aberrant luminal folding, impaired luminal closure, and altered glandular structure in mutant uteri at GD 4.5. Further analysis demonstrated decreased aquaporin-2 (AQP2) expression in mutant mouse uteri during diestrus. Moreover, we provide evidence for altered PCP via dysregulation of cellular architecture, altered E-cadherin expression and localization, and aberrant gene expression in nonpregnant and GD 3.5 mutant mice. Additionally, the loss of PRICKLE1 in endometrial epithelium shows evidence of epithelial-to-mesenchymal transition within luminal epithelial cells of nonpregnant mice, providing a connection to uterine pathologies. Finally, the loss of PRICKLE1 in endometrial epithelium shows alterations to the plane of cellular division, resulting in asymmetric cell division, increased multinucleated cells, and providing a connection to the evidence of epithelial–mesenchymal transition (EMT). PRICKLE1 involvement in the PCP pathway within the uterus and during embryo implantation unveils a complex interplay between molecular cues and cellular responses vital for successful pregnancy establishment.

Results

cKO of *Prickle1* in mouse endometrial epithelium leads to alterations in luminal folding, intrauterine fluid resorption, and decreased embryo implantation

Using *Prickle1*$^{f/+}$ ES cells, we developed *Prickle1*$^{f/f}$ mice and utilized *Lactoferrin-iCre* (24) to conditionally ablate *Prickle1* in the mouse endometrial epithelium (Fig. 1A–D, Fig. S1).

To investigate the impact that the loss of PRICKLE1 within the endometrial epithelium had on fertility, *Prickle1*$^{f/f}$ *Ltf*$^{+/icre}$ cKO female mice were bred with C57BL6 wild type (WT) male mice and the number of live birth pups was tracked following a positive vaginal plug formation. These fertility trials indicated that *Prickle1*$^{f/f}$ *Ltf*$^{+/icre}$ cKO mice have a reduced litter size of 5.70 pups per litter compared with 9.36 pups per litter in *Prickle1*$^{f/f}$ control mice ($P < 0.0001$) (Fig. 1E). However, a wide range of litter sizes was observed within the cKO groups, indicating that *Prickle1*$^{f/f}$ *Ltf*$^{+/icre}$ cKO mice may have a range in the severity of knockout. Therefore, implantation studies were performed at GD 4.5 (where the morning of positive vaginal plug formation was considered GD 0.5) following breeding with C57BL6 WT male mice to investigate the timing of proposed improper embryo implantation. These studies demonstrated that *Prickle1*$^{f/f}$ *Ltf*$^{+/icre}$ cKO mice show two distinct mutant groups: one group with implantation site number similar to that of control mice and one group with no implantation sites present at GD 4.5 (Fig. 1F–J), potentially resulting from the incomplete penetrance of *iCre* expression (25). The results showing a range of live births from *Prickle1*$^{f/f}$ *Ltf*$^{+/icre}$ cKO females (Fig. 1E) indicate further loss of embryos during pregnancy, in addition to the implantation defects.

Past studies have examined the importance of luminal folding during periimplantation to the success of embryo implantation and decidualization (4, 26). To further investigate how the mutant's uterine structures and luminal folding may differ from control mice, 3D imaging of full uterine horns with GD 4.5 implantation sites was performed (Fig. 1K and L). This imaging confirmed the presence of two types of mutants where one set of *Prickle1*$^{f/f}$ *Ltf*$^{+/icre}$ uteri have normal embryos present, normal luminal closure, and normal transverse luminal folding and decidual sites comparable to control mice, while the other set of *Prickle1*$^{f/f}$ *Ltf*$^{+/icre}$ uteri have no embryos present, a completely open lumen, aberrant uterine folding, and no decidua. These more severe mutant mice demonstrate a superfolded luminal nature, indicating improper luminal folding and closure during periimplantation.

Several studies have demonstrated the involvement of aquaporins in the luminal closure and their dynamic regulation during implantation (27–29). Immunostaining of nonpregnant mice at diestrus as well as GD 3.5 *Prickle1*$^{f/f}$ *Ltf*$^{+/icre}$ uteri demonstrated areas of altered AQP2 expression as compared to control uteri (Fig. 1M, Fig. S2). Moreover, a receptive uterus is marked by the downregulation of *Muc-1* in the luminal epithelium and the cessation of epithelial cell proliferation prior to implantation (30–32). It has been well established that the persistent expression of *Muc-1* and stromal growth factors impede implantation (33). Here, we see an increase of fibroblast growth factors *Fgf1*, *Fgf2*, *Fgf7*, *Fgf9*, *Fgf10*, and *Fgf18* in addition to *Muc-1* mRNA expression in the *Prickle1*$^{f/f}$ *Ltf*$^{+/icre}$ cKO when compared with control (Fig. S3). In addition, we see altered expression of *Pgr* and *Esr1* across all estrus cycle stages (Fig. S4) and increased *Pgr*, *Esr1*, and *Muc-1* at GD 4.5 (Fig. S5), indicating aberrant steroid hormone signaling and altered epithelial–stromal crosstalk. Further investigation of steroid hormone signaling indicated increased expression of progesterone receptor (PGR) and estrogen receptor (ER) within the stroma with decreased HAND2 expression (Fig. S6). Moreover, TaqMan analysis revealed increased expression of estrogen-responsive genes, *Greb1*, *Clca1*, and *C3*, and progesterone-responsive genes, *Ihh*, *Areg*, *Cyp26a1*, and *Il13ra2* (Fig. S7). Steroid hormone assessment of cKO in diestrus was comparable to controls (Fig. S8).

While evidence of luminal epithelial changes was seen within the *Prickle1*$^{f/f}$ *Ltf*$^{+/icre}$ uteri, the glandular epithelium remained largely intact but showed altered gland length in 3D (Fig. 2A–D).

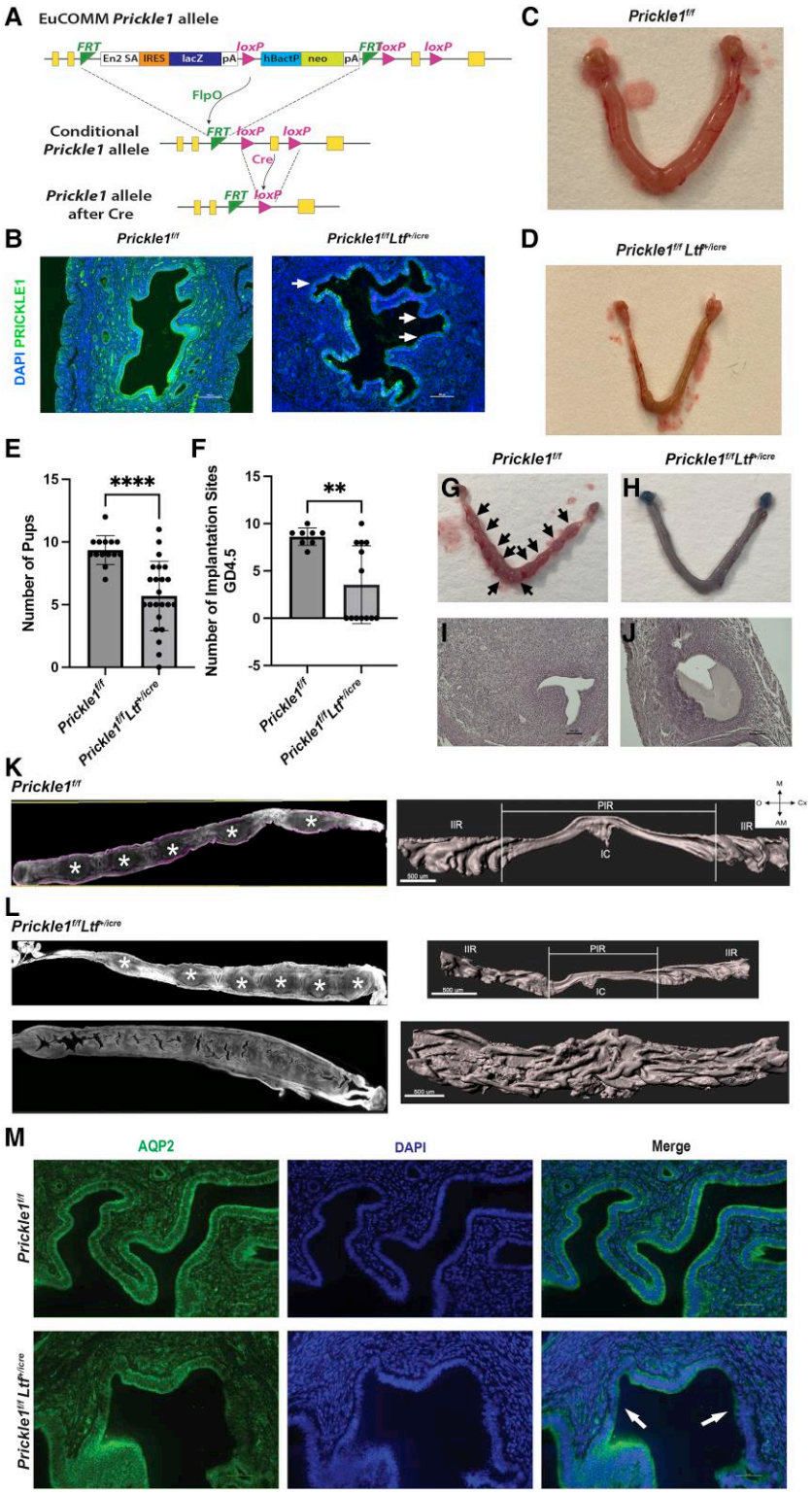

Fig. 1. *Prickle1* cKO in mouse endometrial epithelium displays alterations to luminal folding and decreased embryo implantation. A) *Prickle1*$^{f/f}$ targeting construct. B) Uterine cross-sections of 6-month-old *Prickle1*$^{f/f}$ *Ltf*$^{+/icre}$ cKO and control mice in diestrus stained for PRICKLE1 and DAPI. Arrows indicate areas of patchy PRICKLE1 expression (scale bar, 100 μm). C, D) Representative images showing altered morphology of uterus in 6-month-old *Prickle1*$^{f/f}$ *Ltf*$^{+/icre}$ cKO mouse (D) compared with control (C) mouse during diestrus. E) Fertility assessment in control ($n = 14$) and *Prickle1*$^{f/f}$ *Ltf*$^{+/icre}$ cKO ($n = 23$) 6-month-old mice showing decreased fertility in *Prickle1*$^{f/f}$ *Ltf*$^{+/icre}$ cKO. F) Implantation assessment at GD 4.5 of control ($n = 8$) and *Prickle1*$^{f/f}$ *Ltf*$^{+/icre}$ cKO ($n = 13$) 6-month-old mice indicated two distinct groups of mutants. $^{**}P < 0.05$, $^{****}P < 0.0001$. G–J) Representative images showing implantation sites with corresponding H&E stain in 6-month-old *Prickle1*$^{f/f}$ *Ltf*$^{+/icre}$ cKO mouse (H and J) compared with control (G and I) mouse at GD 4.5 showing abnormal fluid accumulation at proposed embryo site of *Prickle1*$^{f/f}$ *Ltf*$^{+/icre}$ cKO. Arrows indicate embryo implantation sites (scale bar, 100 μm). K, L) Optical z slice showing one horn of *Prickle1*$^{f/f}$ *Ltf*$^{+/icre}$ cKO (L) and control uteri (K) with GD 4.5 embryos (asterisks) with corresponding 3D surface models showing aberrant luminal folding in the mutant with no embryos present (scale bar, 500 μm). PIR, periimplantation region; IIR, interimplantation region; IC, implantation chamber; M, mesometrial pole; AM, antimesometrial pole; O, ovary; Cx, cervix. M) Uterine cross-sections of 6-month-old *Prickle1*$^{f/f}$ *Ltf*$^{+/icre}$ cKO and control mice in diestrus stained for AQP2 and DAPI. Arrows indicate areas of low AQP2 expression (scale bar, 50 μm).

At GD 4.5, as observed previously, glands were tubular and branched in control uteri with a median gland length of 353.62 μm (13, 34). While the glands of the *Prickle1*$^{f/f}$ *Ltf*$^{+/icre}$ cKO mice uteri appeared similar to control uteri with respect to their tubular and branched nature, the glands of mutant uteri that displayed open lumens were significantly shorter in length (median = 292.87 μm) and glands of the mutant uteri that displayed closed lumens showed an increase in length (median = 440.92 μm) (Fig. 2C and D).

cKO of *Prickle1* in mouse endometrial epithelium leads to changes in epithelial architecture and promotes EMT

To further elucidate morphological alterations, cross-sections of *Prickle1*$^{f/f}$ *Ltf*$^{+/icre}$ uteri were examined and revealed prominent areas with aberrant epithelial cell shape and presence of multinucleated cells (Fig. 3A, B and E, Fig. S9). Moreover, immunostaining for PCP proteins showed increased overall expression of E-cadherin with increased basal expression as compared to lateral and apical expression in the control uteri across all cycle stages of estrus (Fig. 3C and D, Fig. S10), providing evidence for PCP disruption (35). Furthermore, *Prickle1*$^{f/f}$ *Ltf*$^{+/icre}$ uteri showed increased overall cytokeratin 7 (KRT7) expression (Fig. S11) and increased SOX9 nuclear expression (56.1%) compared with control uteri (31.4%) (Fig. 3F–H), a marker of endometrial hyperplasia and endometriosis (36, 37), demonstrating that the loss of PRICKLE1 in the endometrial epithelium leads to PCP disruption. In addition, these results were consistent at GD 3.5 (Fig. S2), indicating that this altered PCP expression is present both during the cycle and just prior to implantation.

While alterations to structure and function were seen from our analysis of the uterus as a whole tissue, further understanding of individual cellular changes was pertinent. Therefore, to study the

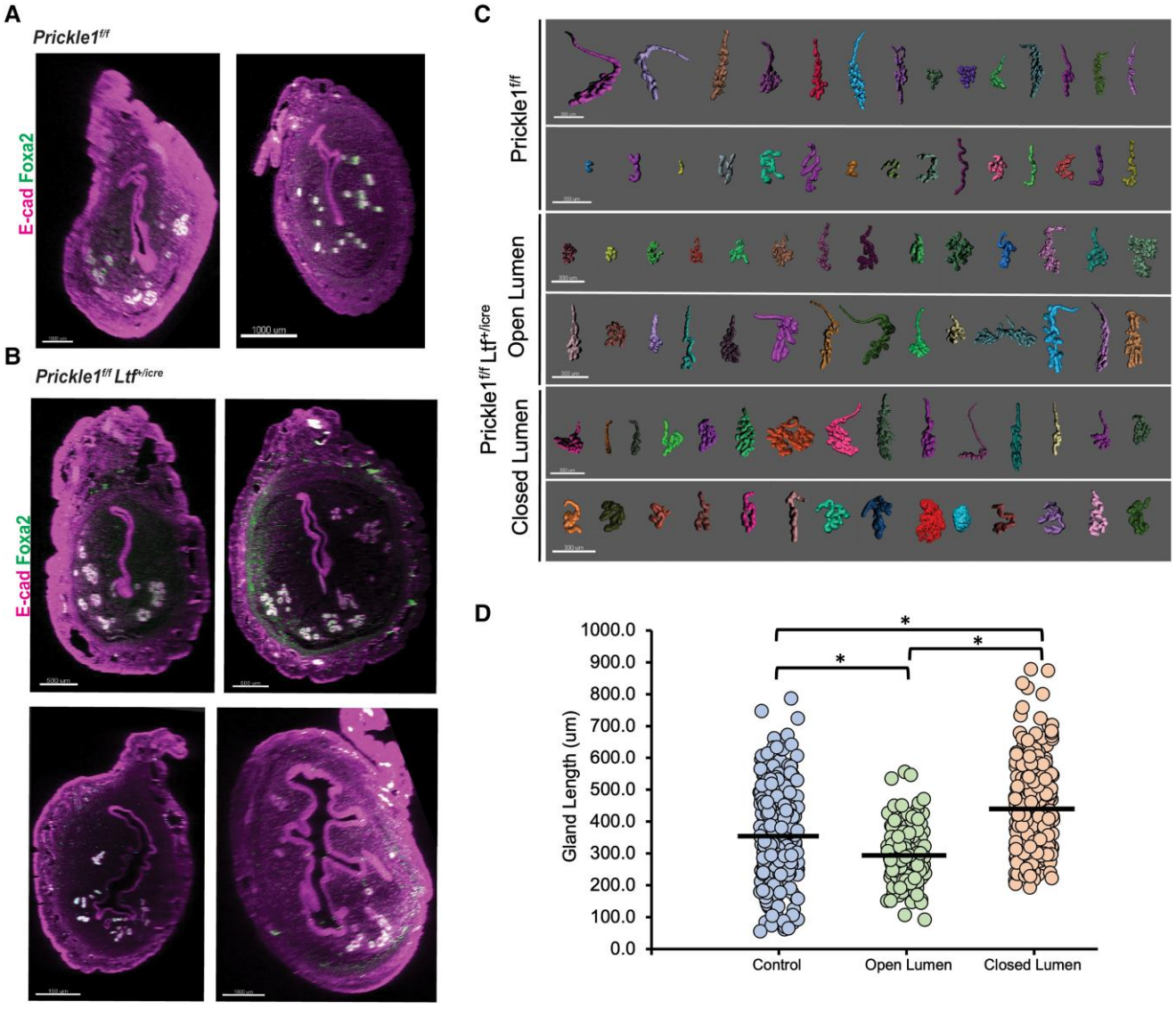

Fig. 2. *Prickle1* cKO in mouse endometrial epithelium do not alter glandular structure at GD 4.5. A, B) Transverse slices of 6-month-old *Prickle1*$^{f/f}$ *Ltf*$^{+/icre}$ cKO (B) compared with control (A) mice at GD 4.5 stained for epithelial marker E-cadherin and glandular marker FOXA2 (scale bars, 500 μm [controls], 1,000 μm [*Prickle1*$^{f/f}$ *Ltf*$^{+/icre}$], 150 μm [*Prickle1*$^{f/f}$ *Ltf*$^{+/icre}$], and 1,000 μm [*Prickle1*$^{f/f}$ *Ltf*$^{+/icre}$]). C) Representative 3D reconstructions of glands of 6-month-old *Prickle1*$^{f/f}$ *Ltf*$^{+/icre}$ cKO compared with control mice at GD 4.5 (scale bars, 300 μm). D) Quantitative analysis of average gland length measurements (each dot represents one gland). 250–470 glands analyzed per mouse. Data analyzed using Kruskal–Wallis test with Dunn's multiple comparisons. *$P < 0.05$.

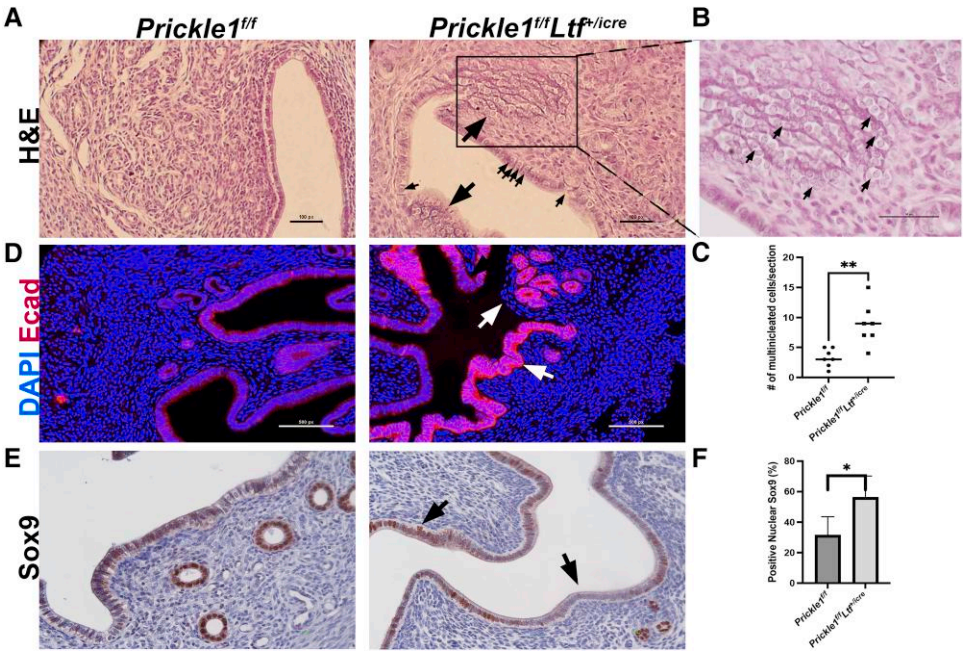

Fig. 3. *Prickle1* cKO in mouse endometrial epithelium leads to altered cellular structure and dysregulation in expression of Wnt/PCP proteins. A, B) H&E stain of 6-month-old *Prickle1*$^{f/f}$ *Ltf*$^{+/icre}$ cKO (B) compared with control (A) in diestrus. Large arrows indicate areas of hyperproliferation and rounded epithelial shape. Small arrows indicate multinucleated cells (scale bars, 100 μm). (B inset) Callout of *Prickle1*$^{f/f}$ *Ltf*$^{+/icre}$ cKO highlights area of multinucleated and spindle-shaped cells. Arrows indicate multinucleated and spindle-shaped cells (scale bars, 50 μm). C, D) Immunofluorescence stain of 6-month-old *Prickle1*$^{f/f}$ *Ltf*$^{+/icre}$ cKO (C) compared with control (D) in diestrus for epithelial marker E-cadherin and DAPI indicating high basolateral and overall E-cadherin expression in mutant. Arrows indicate area of missing epithelium and high basal expression of E-cadherin (scale bars, 500 μm). E) Quantification of multinucleated cells in 6-month-old *Prickle1*$^{f/f}$ *Ltf*$^{+/icre}$ cKO ($n = 7$) compared with control ($n = 7$) in diestrus. $^{**}P < 0.005$. F, G) Immunohistochemistry stain of 6-month-old *Prickle1*$^{f/f}$ *Ltf*$^{+/icre}$ cKO (G) compared with control (F) in diestrus for SOX9. Arrows indicate areas of nuclear expression and multinucleated cells in the mutant (scale bars, 10 μm). H) Quantification of positive SOX9 nuclear staining in 6-month-old *Prickle1*$^{f/f}$ *Ltf*$^{+/icre}$ cKO ($n = 5$) compared with control ($n = 5$) in diestrus. $^{*}P < 0.05$.

impact the loss of PRICKLE1 in the endometrial epithelium has on the whole uterus by cell type, single-cell RNA (scRNA) sequencing was performed on 6-month-old *Prickle1*$^{f/f}$ *Ltf*$^{+/icre}$ and *Prickle1*$^{f/f}$ mice in diestrus (GSE272552 (38)). Six-month-old mice were chosen for this experiment due to the pubertal expression of Ltf-iCre to ensure that the progression epithelial phenotype would be evident in the uteri of cKO mice. Results from Seurat scRNA sequencing data analysis (39), which passed the quality control markers before being analyzed (Fig. S12), identified 12 clusters in the uterus based on their expression profiles (Fig. 4A). Cell types were determined via gene expression profiles using SingleR software (40) and expert curation. Based on conserved gene expression, clusters were identified as stromal (clusters 0, 4, and 5) and epithelial (clusters 3 and 8) (Figs. S13 and S14).

A χ^2 test of homogeneity comparing *Prickle1*$^{f/f}$ *Ltf*$^{+/icre}$ and *Prickle1*$^{f/f}$ scRNA sequencing counts revealed significant differences in populations of myometrial cells, epithelial cells, stromal cells, and natural killer (NK) cells (Fig. S15). Of particular interest was an over 11 times decrease in the number of epithelial cells in the *Prickle1*$^{f/f}$ *Ltf*$^{+/icre}$ group as compared to the control, indicating a loss of epithelial-identified cells within the cKO group. A corresponding increase in stromal cells (clusters 0, 4, and 5) was observed. Moreover, there was four times increase in the number of NK cells present in the cKO when compared with the control.

Top principal component analysis (PCA) features for each cluster were identified and revealed increased REST target genes for clusters 0, 4, and 5 (stromal cells) (41) in addition to increased expression of various collagens (*Col1a1*, *Col1a2*, *Col6a1*, *Col6a3*, *Col6a2*, *Col4a1*, and *Col3a1*) and known markers of EMT (*Serpinh1*, *Ccn1*, *Lum*, *Mmp19*, *Lif*, and *Igfbp6*) (42–47) within the *Prickle1*$^{f/f}$ *Ltf*$^{+/icre}$ group compared with control (Figs. S16 and S17). In addition to PCP, PRICKLE1 is known to regulate the nuclear localization of REST (48).

In addition, decreased expression of *Cdh1*, *Muc1*, and *Tjp3* in epithelial cells was seen, while increased stromal expression of *Dvl1*, *Wnt5a*, *Tjp1*, *Tjp2*, and *Esr1* was seen (Fig. S18). These results indicate that prominent changes are occurring within the stromal cell population of the *Prickle1*$^{f/f}$ *Ltf*$^{+/icre}$ cKO mice due to the loss of PRICKLE1 within the endometrial epithelium. Furthermore, the gene expression profile of the epithelial cluster of the cKO showed similarities to cancer, organismal injury and abnormalities, reproductive system disease, and cell-to-cell signaling (Tables 1 and 2, Tables S1–S4), while stromal clusters of the cKO showed many of the same pathways in addition to inflammatory response, cellular movement, tissue morphology, and reproductive system development and function (Table 3, Tables S5–S12). Moreover, the gene expression profile of the NK cell cluster of the cKO showed connections to cancer, inflammatory disease, cell cycle, cellular growth and proliferation, and tissue development (Tables S13–S15).

In addition, a loss of cells within clusters 3 and 8 (epithelial cells) with a corresponding increase in cells within clusters 0, 4, and 5 (stromal cells) was observed within the *Prickle1*$^{f/f}$ *Ltf*$^{+/icre}$ group as compared to the control group (Fig. 4B and C, Fig. S15). Given the previous evidence of altered gene expression and EMT markers in the stroma, we hypothesized that these epithelial groups were potentially undergoing EMT and re-clustering as stroma in the *Prickle1*$^{f/f}$ *Ltf*$^{+/icre}$ cKO uteri. RNA velocity analysis was performed to identify high-dimensional vectors to predict the future state of the cells on a pseudo timescale (49) (Fig. S19). Immediately, high velocity (as indicated by the higher ratio of unspliced/spliced RNA transcripts) was seen in clusters 0, 4, and 5 of

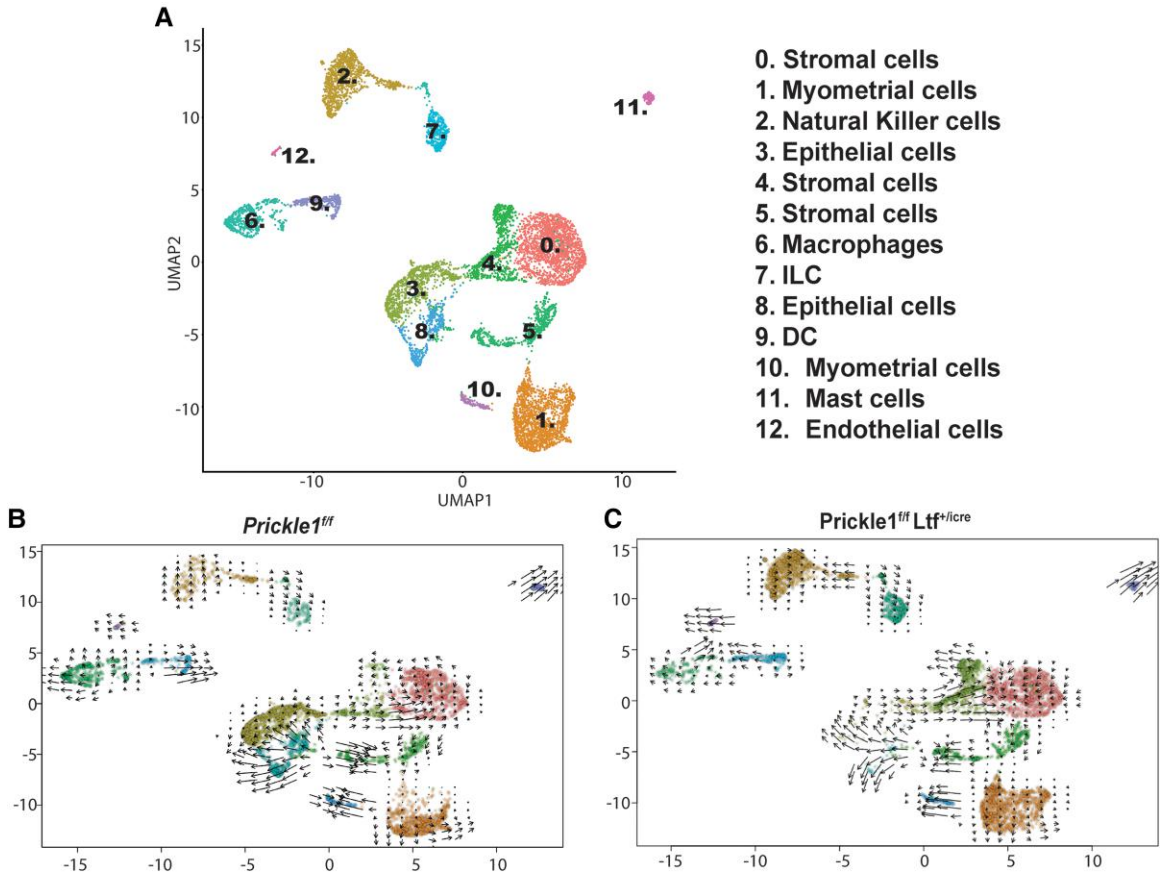

Fig. 4. *Prickle1* cKO in mouse endometrial epithelium leads to increased expression of collagens, Wnt/PCP, and EMT markers in stromal clusters (0, 4, and 5). A) SingleR program predictions for cell clusters present in control and *Prickle1*$^{f/f}$ *Ltf*$^{+/icre}$ mice uteri shown by a uniform manifold approximation projection (UMAP) plot. Cell clusters were given a number between 0 and 12. B, C) Velocity RNA analysis embedding stream for control (B) and *Prickle1*$^{f/f}$ *Ltf*$^{+/icre}$ (C) showing higher magnitude velocity in epithelial cells (cluster 3) of *Prickle1*$^{f/f}$ *Ltf*$^{+/icre}$ mice.

Table 1. Pathway analysis of predicted molecular and cellular functions associated with dysregulated genes in the epithelial cell population (cluster 3) of Prickle1$^{f/f}$ Ltf$^{+/icre}$ cKO mice.

Molecular and cellular functions	*P*-value
Cellular movement	4.82E−61
Cell death and survival	1.19E−47
Cellular development	4.12E−37
Cellular growth and proliferation	4.12E−37
Cell-to-cell signaling and interaction	1.22E−34

Function predictions made by IPA software based off genes which were found to be dysregulated in epithelial cells of 6-month-old *Prickle1*$^{f/f}$ *Ltf*$^{+/icre}$ mice cKO ($n = 3$) in diestrus.

Table 2. Pathway analysis of predicted disease and disorders associated with dysregulated genes in the epithelial cell population (cluster 3) of Prickle1$^{f/f}$ Ltf$^{+/icre}$ cKO mice.

Disease and disorders	*P*-value
Cancer	7.29E−54
Organismal injury and abnormalities	7.29E−54
Reproductive system disease	1.51E−45
Gastrointestinal disease	7.73E−42
Respiratory disease	5.73E−38

Disease predictions made by IPA software based off genes which were found to be dysregulated in epithelial cells of 6-month-old *Prickle1*$^{f/f}$ *Ltf*$^{+/icre}$ mice cKO ($n = 3$) in diestrus.

the stroma of *Prickle1*$^{f/f}$ *Ltf*$^{+/icre}$ cKO uteri as predicted, indicating large changes to the RNA transcripts of this group of cells in comparison with their control counterparts (Fig. 4B and C, Fig. S19).

To further demonstrate that this reclassification of cells is due to EMT, RNA velocity analysis of 120 EMT hallmark genes revealed high velocity in clusters 3 and 8 (epithelial) to clusters 0, 4, and 5 (stroma) within the *Prickle1*$^{f/f}$ *Ltf*$^{+/icre}$ cKO group when compared with the control group (Fig. S1A–L). These results provide evidence that *Prickle1* knockout in the endometrial epithelium promotes EMT within the epithelial cells and potentially reclassifies these cells as stromal cells during scRNA sequencing analysis.

To further validate the results of the RNA velocity analysis, immunostaining of EMT markers known to be up-regulated in endometrial cancers (45, 50, 51) was performed on *Prickle1*$^{f/f}$ *Ltf*$^{+/icre}$ uteri cross-sections. Increased expression of ZEB1 (Fig. S20A), TWIST1 (Fig. S20B), SNAI2/SLUG (Fig. S20C), and vimentin (Fig. S20D) in both the endometrial epithelium and stroma of the cKO when compared with control uteri was observed, confirming evidence of increased EMT activity within the *Prickle1*$^{f/f}$ *Ltf*$^{+/icre}$ cKO as previously seen by the scRNA sequencing analysis and providing further evidence for the loss of PRICKLE1 in promoting EMT with the endometrial epithelium.

cKO of *Prickle1* in mouse endometrial epithelium leads to altered plane of epithelial cell division

Further evaluation of the binuclear and multinucleated epithelial layer revealed alterations to the plane of cell division within

Table 3. Pathway analysis of predicted disease and disorders associated with dysregulated genes in the stromal cell population (cluster 4) of Prickle1$^{f/f}$ Ltf$^{+/icre}$ cKO mice.

Disease and disorders	P-value
Cancer	1.20E−26
Organismal injury and abnormalities	1.20E−26
Gastrointestinal disease	1.28E−18
Endocrine system disorders	9.03E−17
Reproductive system disease	1.97E−11

Disease predictions made by IPA software based off genes which were found to be dysregulated in stromal cells of 6-month-old *Prickle1*$^{f/f}$ *Ltf*$^{+/icre}$ mice cKO ($n = 3$) in diestrus.

the *Prickle1*$^{f/f}$ *Ltf*$^{+/icre}$ uteri cross-sections with asymmetric epithelial cell division seen in the absence of PRICKLE1 (Fig. 5A–D). *Prickle1*$^{f/f}$ *Ltf*$^{+/icre}$ uteri contained much higher rates of asymmetric epithelial cell division in comparison with controls (Table S16). Moreover, higher levels of E-cadherin expression were present at basal and apical sides of the epithelium within the cKO uteri compared with controls, providing a potential mechanism for altered polarity and incomplete cell division (Fig. 5D and E). Finally, during scRNA data analysis, *Prickle1*$^{f/f}$ *Ltf*$^{+/icre}$ cKO samples demonstrated a statistically higher occurrence of doublets (3.4%) as compared to control samples (2.5%) ($P < 0.05$) (Table S17), indicating a higher percentage of multinucleated cells present within the cKO samples, while assessment of apoptosis did not show any statistical difference between control and mutant (Fig. S21).

Discussion

The mechanisms that regulate the unicellular layer architecture of endometrial luminal epithelium, timing, and cycle of the uterine receptive state for proper embryo implantation are poorly understood. In addition, although some recent advancements in understanding PCP-related functions within the uterus have been made (14), the specific role of PCP pathway in uterine epithelial morphogenesis and embryo implantation has previously been understudied. Here, we demonstrate the importance of PRICKLE1 in uterine endometrial epithelial architecture, embryo implantation, fertility, and overall uterine physiology using a *Prickle1* endometrial epithelial cKO mouse model.

We observed two distinct sets of phenotypes related to fertility in PRICKLE1 mutants, with a more severe mutant phenotype exhibiting no implantation sites and a less severe mutant with implantation sites similar to the control at GD 4.5 but with lower live pups at birth. Previous work with *Lactoferrin-iCre* has demonstrated known variability in the expression, leading to variability excision within mutants (25). The more severe mutants also displayed aberrant luminal folding, an open lumen, and altered AQP2 expression, indicating that *Prickle1*$^{f/f}$ *Ltf*$^{+/icre}$ cKO mice may be unable to remove fluid from the lumen properly, thus preventing luminal closure and inhibiting successful embryo implantation. AQP2 is known to regulate luminal closure (27–29). Moreover, the increased expression of fibroblast growth factors, *Muc-1*, *Pgr*, and *Esr1* (Figs. S3 and S4), coupled with the increased nuclear expression of ER, PGR, and decreased HAND2 in the cKO with increased estrogen and progesterone-responsive genes (Figs. S6 and S7), is consistent with results suggesting an impairment in the crosstalk between stroma and epithelium via Hand2 and progesterone (33). Decreased litter size even in mice that show normal implantation numbers at GD 4.5 may indicate this altered epithelial–stromal crosstalk affects maintenance of pregnancy. The role of PRICKLE1 in epithelial–stromal communication and steroid hormone signaling needs further investigation.

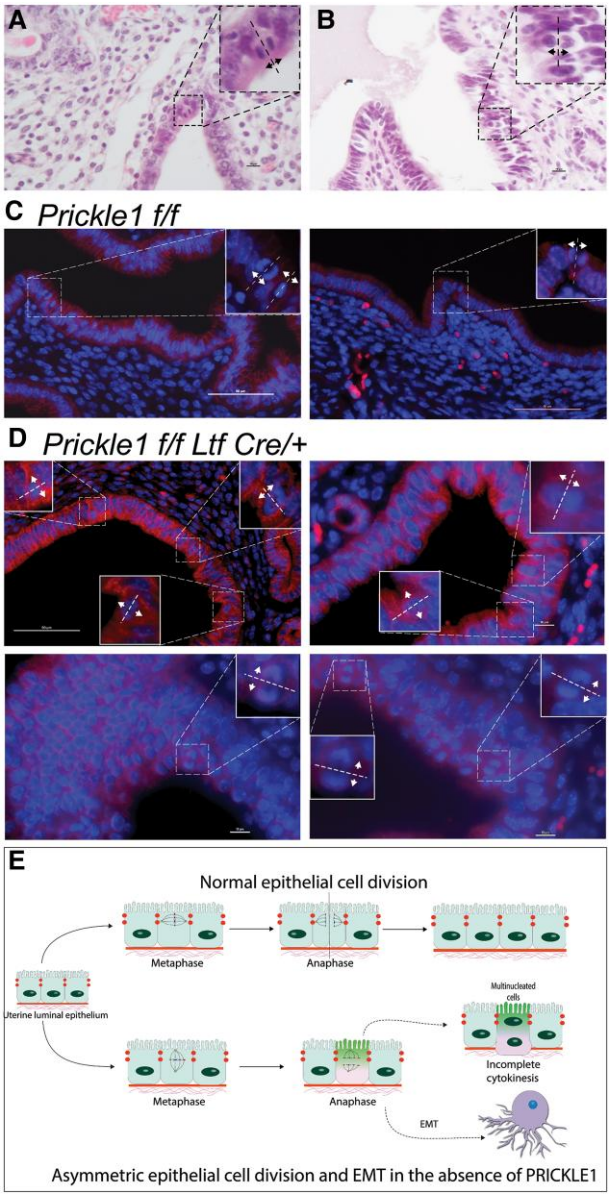

Fig. 5. *Prickle1* cKO in mouse endometrial epithelium displays disruption in the polarity of cell division. A, B) H&E stain of 6-month-old *Prickle1*$^{f/f}$ *Ltf*$^{+/icre}$ cKO (B) compared to control (A) in diestrus. Callouts highlight dividing cells with altered orientation in the *Prickle1*$^{f/f}$ *Ltf*$^{+/icre}$ cKO (scale bars, 10 μm). C) Immunofluorescence stain of 6-month-old *Prickle1*$^{f/f}$ controls in diestrus for epithelial marker E-cadherin and DAPI. Callouts highlight dividing cells with normal orientation (scale bars, 50 μm). D) Immunofluorescence stain of 6-month-old *Prickle1*$^{f/f}$ *Ltf*$^{+/icre}$ cKO mice in diestrus for epithelial marker E-cadherin and DAPI. Callouts highlight dividing cells with altered orientation (scale bars, 50 μm). E) Longitudinal view schematic depicting normal epithelial cell division and asymmetric epithelial cell division in the absence of PRICKLE1.

Immunostaining of *Prickle1*$^{f/f}$ *Ltf*$^{+/icre}$ uteri for E-cadherin and FOXA2 demonstrated glandular structure consistent with pregnancy at GD 4.5 (Fig. 2C), even with an open lumen in the mutants that did not contain any positive embryo implantation sites. These results indicate that the inability of the lumen to fold and close properly, in addition to dysregulated cellular communication, may be responsible for the embryo implantation failure within these mice that otherwise should have been pregnant.

Although the structure of the uterine glands of the mutant uteri appeared similar to the tubular and branched glands of control uteri, there were differences in the gland length that correlated with the open or closed luminal phenotype (Fig. 2C and D). The potential role of PRICKLE1 in regulating uterine gland morphogenesis needs further characterization.

Our scRNA sequencing analysis demonstrates how the loss of PRICKLE1 in the endometrial epithelium alters uterine gene expression and provides evidence for decreased number of cells with epithelial phenotype in the cKO with an increase in stromal cell numbers. Furthermore, RNA velocity analysis indicates a potential transition of epithelial cells into clusters with stromal-like gene expression. It has been well established that EMT is a contributor to several endometrial diseases, including endometriosis, adenomyosis, and endometrial cancers (52–54). Our data indicate a possible role for the loss of PRICKLE1 in EMT. In addition to the changes in epithelial and stromal cells in the cKO uteri, the scRNA data showed a significant increase in NK cells (Fig. S15C). The overabundance of NK cells in the cKO provides a potential connection to the fertility and implantation phenotype as it has been shown that uterine NK cell population dysregulation is connected to recurrent miscarriage, fertility, and uterine disorders such as endometriosis (55–57).

Spatial cues that organize a unicellular 2D sheet of epithelium in a plane orthogonal to the apical–basal polarity are regulated locally through various Wnt/PCP signaling molecules (58). Additionally, symmetric (conservative) cell division in the epithelium is essential to maintain the apical–basal polarity and proper epithelial function, including implantation (4, 58). Our data indicating the presence of binucleated and multinucleated cells in the luminal epithelium, along with altered plane of cell division, indicate a crucial role for PRICKLE1 in maintaining conservative, symmetrical cell division in the epithelium and potentially in the maintenance of unicellular layer architecture. The presence of binucleated cells in the luminal epithelium may indicate incomplete cytokinesis or endoreduplication in cells (59). Proper cytokinesis requires the formation of a contractile ring at the site of E-cadherin expression (58). Therefore, increased basal E-cadherin expression and an altered mitotic plane of division support incomplete cytokinesis in our cKO. In this regard, regulation of expression and localization of E-cadherin by PRICKLE1 might hold the key for altered epithelial architecture and function. Furthermore, multinucleated spindle-shaped cells in the cKO epithelium may indicate that both defective cytokinesis and endoreduplication might be present (59). This observation, further strengthened by the increased number of doublets removed during scRNA data analysis in the cKO (Table S16), is unique compared with the loss of other PCP genes such as *Vangl2*, *Ror2*, and *Wnt5a* (60, 61). Loss of these PCP genes has shown varying degrees of uterine epithelial subcellular changes as well as implantation defects. However, none of these genes have shown a dramatic loss of polarity of cell division or incomplete cytokinesis in the uterus. Moreover, the role of asymmetric cell division which gives rise to two daughter cells with distinct fates in EMT has been reported (62). Whether the altered plane of cell division observed in the cKO endometrium has a direct role in the dramatic increase in EMT is unclear at this point.

Materials and methods

Generation of *Prickle1* cKO mouse

Mouse embryonic stem cell clones harboring floxed *Prickle1* (*Prickle1tm1a(EUCOMM)Wtsi*, ES cell clones with cKO potential, targeting vector HTGR03009_Z_6_E08) were acquired from EuCOMM. The ES cells were used to generate chimeric founder mice, which were mated to C57BL6 WT mice to create heterozygous $Prickle1^{f/+}$ mice. These mice were crossed with FLPo (Gt(ROSA)26Sor$^{tm2(FLP*)Sor}$) mice (JAX stock #009086) to remove FRT flanked bgalneo sequences (63). These were bred together to obtain homozygous $Prickle1^{f/f}$ mice, which were then crossed with transgenic *Lactoferrin-iCre* mice (24). The mice were genotyped by PCR using primers for *Prickle1* (5′GGTTTCATGTGTTGAGACATTTC) (5′GTATTTCTGTGC CCTTTTTGTCGTCG) (5′TGAACTGATGGCGAGCTCAGACC) as well as primers for $Ltf^{+/icre}$ (5′AACTAGCACACCTGGTTGAGG) (5′CTTC TTGGGAGGCAGTGAAC) (5′CAGGTTTTGGTGCACAGTCA). All experiments involving animals were conducted in accordance with protocols reviewed and approved by the KUMC Institutional Animal Care and Use Committee (IACUC) (Animal Care and Use Protocol number: 23-02-296).

Fertility and implantation

Female $Prickle1^{f/f}$ $Ltf^{+/icre}$ and $Prickle1^{f/f}$ mice were mated with C57BL6 WT males to induce pregnancy. The morning of finding the vaginal plug was considered day 0.5 of pregnancy. Litter size analysis was tracked via number of pups born following positive vaginal plug formation at days 17–21. Implantation was assessed by sacrificing pregnant dams on day 3.5 or 4.5 following 100 μL intravenous injection of 1% Chicago Sky Blue 6B dye (Millipore Sigma, Cat# C8679) solution and counting the number of distinct blue bands present within the uterus.

Whole-mount immunofluorescence, confocal imaging, and image analysis

Whole-mount immunofluorescence was performed as previously described (13). GD 4.5 $Prickle1^{f/f}$ and $Prickle1^{f/f}$ $Ltf^{+/icre}$ *uteri* were dissected from mice and fixed in DMSO/methanol (1:4). Subsequently, they were rehydrated in a methanol/PBST (1% Triton X-100 in phosphate-buffered saline [PBS]) (1:1) solution for 15 min, followed by a phosphate-buffered saline with Tween (PBST) wash for 15 min. Uteri were then incubated in a blocking solution (2% powdered milk in PBST) for 1 h at room temperature. They were incubated with primary antibodies diluted in blocking solution for nine nights at 4 °C. Primary antibodies included rabbit anti-FOXA2 (Abcam, ab108422; 1:300) and rat anti-CDH1 (M108, Takara Biosciences, 1:500). Uteri were washed once for 15 min with 1% PBST followed by four additional PBST washes for 45 min each at room temperature. Uteri were then incubated with 1:500 Alexa Fluor 555 donkey antirabbit IgG (Invitrogen, A31572), Alexa Fluor 633 goat antirat IgG (Invitrogen, A21094), and Hoechst (Sigma-Aldrich, B2261) at 4 °C for three nights. Samples were washed once for 15 min and three more times for 45 min each with 1% PBST and then stepwise dehydrated into 100% methanol. Uteri were incubated overnight at 4 °C in a 3% H_2O_2 solution prepared in methanol. Next day, the samples were washed twice for 15 min each and a final 1-h wash with 100% methanol at room temperature and then cleared in benzyl alcohol/benzyl benzoate (1:2, BABB) (Sigma-Aldrich, 108006, B6630) overnight.

Confocal imaging

Whole tissue immunofluorescence samples were imaged using a Leica TCS SP8 X Confocal Laser Scanning Microscope System with white-light laser, 10× air objective, and 20× BABB objective. Using the tile scan function with Z stacks 7 μm apart (10×), images covering the entire length and thickness of the uterine horn were acquired. Higher-resolution images of implantation sites and

regions flanking the implantation site were acquired using a 20× BABB objective. The tile scan function was used, and Z stacks 5 μm apart were acquired.

Image analysis

Image analysis was performed using commercial software Imaris v9.2.1 (Bitplane). The confocal image (.LIF) files were imported into the Surpass mode of Imaris. To derive the lumen-only signal, the FOXA2 signal of glands was subtracted from the epithelial CDH1 signal using the channel arithmetic MATLAB-based function (26). 3D renderings were created using automated and manual mode in Surface function for lumen-only and FOXA2 or CDH1 (glands only) signal. Individual glands were then isolated and presented in a comprehensive gallery for visualization using the Imaris Vantage function. Gland length was determined using Bounding Box OOC function in Imaris that measures the shortest straight-line distance from its point of connection to the uterine lumen to the furthest tip. To compare gland length measurements between *Prickle1*$^{f/f}$ mice and *Prickle1*$^{f/f}$ *Ltf*$^{+/icre}$ cKO mice, Kruskal–Wallis test with Dunn's multiple comparisons was performed using R statistical software. A P-value < 0.05 was considered significant, indicating differences between comparisons.

Histology and staining

Uterine tissues were fixed in 4% paraformaldehyde and processed for paraffin embedding. Tissue sections were deparaffinized in xylene, rehydrated using a series of ethanol, and then stained with hematoxylin and eosin (H&E) or immunostained. For immunostaining, antigen retrieval was done using antigen retrieval unmasking solution (Vector Labs, Cat# H-3301) prior to staining.

For immunofluorescence staining, rehydrated tissue sections were stained as previously described (64) using primary antibodies AQP2 (Novus Biologicals, Cat# NB110-74682SS, 1:100), E-CAD (Cell Signaling, Cat# 24E10, 1:100), ZEB1 (Cell Signaling, Cat# 70512, 1:400), TWIST1 (Cell Signaling, Cat# 90445, 1:100), SNAI2 (Cell Signaling, Cat# 9585, 1:100), PGR (Invitrogen, Cat# MA1-411, 1:100), and PRICKLE1 (BiCell Scientific, Cat# 50621, 1:100). Secondary antibodies were obtained from Jackson Immuno Research Laboratories for Alexa Fluor 488 and 594 (Cat# 711-545-152 and 711-585-152, 1:200).

For immunohistochemistry staining, rehydrated samples were prepared using an ABC Universal PLUS Peroxidase kit (Vector Labs, Cat# PK-8200) and then with primary antibodies KRT7 (ThermoFisher Scientific, Cat# pA5-82291, 1:500), SOX9 (Cell Signaling, Cat# 82630, 1:100), vimentin (Cell Signaling, Cat# D21H3, 1:100), ER (Proteintech, Cat# 21244-1-AP, 1:800), and dHAND (Santa-Cruz Biotechnology, Cat# sc-398167, 1:500).

For TUNEL apoptosis staining, rehydrated samples were prepared using a One-Step TUNEL In Situ Apoptosis kit (Elabscience, Cat# E-CK-A320) and then imaged.

RNA isolation and qRT-PCR analysis

Total RNA was isolated from uterine tissue samples stored in RNAlater (Invitrogen, Cat# AM7020) and then biopulverized and placed into TRIzol reagent (Invitrogen, Cat# 15596026). Following TRIzol, a series of chloroform, isopropanol, and ethanol washes were used to isolate the RNA. Following quantification using a Nanodrop spectrophotometer, aliquots of RNA were reverse-transcribed using High-Capacity cDNA Reverse Transcription kit (Applied Biosystems, 4368814). TaqMan assays for *Fgf1* (IDT, Mm.PT.56a.41158563), *Fgf2* (IDT, Mm.PT.56a.5129235), *Fgf7* (IDT, Mm.PT.56a.28834565), *Fgf9* (IDT, Mm.PT.56a.5456225), *Fgf10* (IDT, Mm.PT.58.11905869), *Fgf18* (IDT, Mm.PT.58.14021387), *Muc-1* (IDT, Mm.PT.58.15865847), *Greb1* (IDT, Mm.PT.58.11217662), *Clca3* (IDT, Mm.PT.58.9995580), *C3* (IDT, Mm.PT.58.17325540), *Ihh* (IDT, Mm.PT.58.30489545), *Areg* (IDT, Mm.PT.58.31037760), *Cyp26a1* (IDT, Mm.PT.58.10791878), and *Il13ra2* (IDT, Mm.PT.58.28388240) were used to quantify gene expression differences utilizing the delta delta C(T) method with housekeeping genes Rn18s (ThermoFisher Scientific, Mm03928990_G1).

Hormone assessment

Samples of serum from *Prickle1*$^{f/f}$ *Ltf*$^{+/icre}$ ($n = 4$) and *Prickle1*$^{f/f}$ ($n = 4$) mice aged 4 months were assayed by ELISA at the University of Virginia Center for Research in Reproduction, Ligand Assay and Analysis Core (Charlottesville, VA, USA).

scRNA sequencing

Whole uteri of *Prickle1*$^{f/f}$ *Ltf*$^{+/icre}$ ($n = 3$) and *Prickle1*$^{f/f}$ ($n = 3$) mice aged 6 months were isolated immediately following euthanasia and washed with cold 1× PBS. Uteri were digested as previously described (41), and samples were pooled following digestion. The KUMC genomics core processed and sequenced the cells as previously described (41). The *Prickle1*$^{f/f}$ *Ltf*$^{+/icre}$ sample had 5,805 cells with 70,202 mean reads and 2,078 median genes per cell, while the *Prickle1*$^{f/f}$ sample had 5,426 cells with 43,202 mean reads and 1,098 median genes per cell. Both samples had high sequence saturation levels (>60%), and the mapping rate of reads to the mouse genome (10 mm) was >90% for both samples.

Single-cell data analysis

scRNA sequencing libraries were generated using the 10× Chromium Single Cell 3′ v3 chemistry (10× Genomics) and sequenced in an Illumina NovaSeq 6000 sequencing machine. The raw sequence reads were processed using the 10× Genomics Cellranger pipeline (v 6.1.1) to obtain UMI feature-barcode count matrices. Doublets were removed using DoubletFinder (65) and cells filtered to contain only those cells with at least 500 UMIs and over 250 detected genes with a genes per UMI ratio >0.8 and a mitochondrial gene ratio <20%. The resulting single-cell data were analyzed using the R software Seurat (66) (v4) as previously described (67). The analysis was performed at a 0.4 cluster resolution reasoned using the Clustree software (68) giving 12 stable clusters. The cluster cell types were identified using the SingleR software (40) and our expert curation as previously described (41). Annotations were based on the two reference datasets, ImmGenData from the Immunological Genome Project (ImmGen) (69) and MouseRNAseqData (70). The dynamic progression of transcription in the single-cell data was analyzed using the Velocyto package (49).

Acknowledgments

The authors acknowledge the Transgenic and Gene-Targeting Institutional Facility for help with the transgenic mice, the Genomics Core (Kansas Intellectual and Developmental Disability Research Center [KIDDRC] [NIH U54 HD090216], the Centers of Biomedical Research Excellence [P30 GM122731-03], and the NIH S10 High-End Instrumentation Grant [NIH grants S10 OD021743]) for help with the scRNA sequencing and the KIDDRC (NIH U54 HD 090216) for help with the imaging at the University of Kansas Medical Center, Kansas City, KS 66160, USA. The authors also thank the University of Virginia Center for Reproduction Ligand Assay and Analysis core, supported by NIH/NCTRI P50-HD28934.

Supplementary Material

Supplementary material is available at *PNAS Nexus* online.

Funding

V.M.C. was supported by grants from the National Institute of Child Health and Human Development: R01 HD094373, R01 HD076450, and R01 HD105714-01. R.A. was supported by grants from National Institute of Child Health and Human Development: R01 HD109152. E.R.R. was supported by the Madison and Lila Self Graduate Fellowship. A.V.B. was supported by the Michigan State University, Department of Obstetrics, Gynecology, and Reproductive Biology, Walstrom Family Endowed Women's Health Research Fund.

Author Contributions

V.M.C. and R.A. designed the research. E.R.R., A.V.B., So.G., Su.G., and R.A. performed the research. E.R.R., A.V.B., Su.G., R.A., and V.M.C. analyzed the data. E.R.R., Su.G., A.V.B., R.A., and V.M.C. wrote and edited the manuscript.

Preprints

This manuscript was posted on a preprint: https://doi.org/10.1101/2024.08.06.605120

Data Availability

Upon acceptance of the manuscript for publication, the authors agree to publicly release all data underlying the study. This includes scRNA sequencing data submitted to the NCBI GEO. The codes used for data analysis are included in the Materials and methods section. Data type: scRNA sequencing data. Repository name: NCBI-GEODOI/accession number(s): GSE272552-Token ilmhyswgnnsjpex.

References

1 Ye X. 2020. Uterine luminal epithelium as the transient gateway for embryo implantation. *Trends Endocrinol Metab*. 31(2):165–180.
2 Kalam SN, Dowland S, Lindsay L, Murphy CR. 2018. Microtubules are reorganised and fragmented for uterine receptivity. *Cell Tissue Res*. 374(3):667–677.
3 Moore CL, Cheng D, Shami GJ, Murphy CR. 2016. Correlated light and electron microscopy observations of the uterine epithelial cell actin cytoskeleton using fluorescently labeled resin-embedded sections. *Micron*. 84:61–66.
4 Aplin JD, Ruane PT. 2017. Embryo-epithelium interactions during implantation at a glance. *J Cell Sci*. 130(1):15–22.
5 Murphy CR. 2004. Uterine receptivity and the plasma membrane transformation. *Cell Res*. 14(4):259–267.
6 Zhang Y, *et al.* 2015. Aquaporin-dependent excessive intrauterine fluid accumulation is a major contributor in hyper-estrogen induced aberrant embryo implantation. *Cell Res*. 25(1):139–142.
7 Schjenken JE, Robertson SA. 2014. Seminal fluid and immune adaptation for pregnancy–comparative biology in mammalian species. *Reprod Domest Anim*. 49(Suppl 3):27–36.
8 Sharkey DJ, Glynn DJ, Schjenken JE, Tremellen KP, Robertson SA. 2018. Interferon-gamma inhibits seminal plasma induction of colony-stimulating factor 2 in mouse and human reproductive tract epithelial cells. *Biol Reprod*. 99(3):514–526.
9 Thie M, Fuchs P, Denker HW. 1996. Epithelial cell polarity and embryo implantation in mammals. *Int J Dev Biol*. 40(1):389–393.
10 Johnson GA, Burghardt RC, Bazer FW. 2014. Osteopontin: a leading candidate adhesion molecule for implantation in pigs and sheep. *J Anim Sci Biotechnol*. 5(1):56.
11 Tu Z, *et al.* 2016. Uterine RAC1 via Pak1-ERM signaling directs normal luminal epithelial integrity conducive to on-time embryo implantation in mice. *Cell Death Differ*. 23(1):169–181.
12 Davey CF, Moens CB. 2017. Planar cell polarity in moving cells: think globally, act locally. *Development*. 144(2):187–200.
13 Arora R, *et al.* 2016. Insights from imaging the implanting embryo and the uterine environment in three dimensions. *Development*. 143(24):4749–4754.
14 Yuan J, *et al.* 2016. Planar cell polarity signaling in the uterus directs appropriate positioning of the crypt for embryo implantation. *Proc Natl Acad Sci U S A*. 113(50):E8079–E8088.
15 Jenny A, Mlodzik M. 2006. Planar cell polarity signaling: a common mechanism for cellular polarization. *Mt Sinai J Med*. 73(5):738–750.
16 Jenny A, Reynolds-Kenneally J, Das G, Burnett M, Mlodzik M. 2005. Diego and Prickle regulate frizzled planar cell polarity signalling by competing for dishevelled binding. *Nat Cell Biol*. 7(7):691–697.
17 Seifert JR, Mlodzik M. 2007. Frizzled/PCP signalling: a conserved mechanism regulating cell polarity and directed motility. *Nat Rev Genet*. 8(2):126–138.
18 Wang Y, Nathans J. 2007. Tissue/planar cell polarity in vertebrates: new insights and new questions. *Development*. 134(4):647–658.
19 Tao H, *et al.* 2009. Mouse prickle1, the homolog of a PCP gene, is essential for epiblast apical-basal polarity. *Proc Natl Acad Sci U S A*. 106(34):14426–14431.
20 Tao H, *et al.* 2012. Nuclear localization of Prickle2 is required to establish cell polarity during early mouse embryogenesis. *Dev Biol*. 364(2):138–148.
21 Yang T, Bassuk AG, Fritzsch B. 2013. Prickle1 stunts limb growth through alteration of cell polarity and gene expression. *Dev Dyn*. 242(11):1293–1306.
22 Yang T, *et al.* 2014. Analysis of PRICKLE1 in human cleft palate and mouse development demonstrates rare and common variants involved in human malformations. *Mol Genet Genomic Med*. 2(2):138–151.
23 Liu C, *et al.* 2014. Null and hypomorph Prickle1 alleles in mice phenocopy human Robinow syndrome and disrupt signaling downstream of Wnt5a. *Biol Open*. 3(9):861–870.
24 Daikoku T, *et al.* 2014. Lactoferrin-iCre: a new mouse line to study uterine epithelial gene function. *Endocrinology*. 155(7):2718–2724.
25 Wang P, *et al.* 2018. Generation of mouse for conditional expression of forkhead box A2. *Endocrinology*. 159(4):1897–1909.
26 Madhavan MK, *et al.* 2022. Aberrant uterine folding in mice disrupts implantation chamber formation and alignment of embryo-uterine axes. *Development*. 149(11):dev200300.
27 Jablonski EM, McConnell NA, Hughes FM Jr, Huet-Hudson YM. 2003. Estrogen regulation of aquaporins in the mouse uterus: potential roles in uterine water movement. *Biol Reprod*. 69(5):1481–1487.
28 de Oliveira V, *et al.* 2020. Uterine aquaporin expression is dynamically regulated by estradiol and progesterone and ovarian stimulation disrupts embryo implantation without affecting luminal closure. *Mol Hum Reprod*. 26(3):154–166.
29 Im JW, Lee CY, Kim DH, Bae HR. 2020. Differential expressions of aquaporin subtypes in female reproductive tract of mice. *Dev Reprod*. 24(3):177–185.
30 Surveyor GA, *et al.* 1995. Expression and steroid hormonal control of Muc-1 in the mouse uterus. *Endocrinology*. 136(8):3639–3647.

31 Finn CA, Martin L. 1974. The control of implantation. *J Reprod Fertil*. 39(1):195–206.
32 Carson DD, *et al.* 2000. Embryo implantation. *Dev Biol*. 223(2): 217–237.
33 Li Q, *et al.* 2011. The antiproliferative action of progesterone in uterine epithelium is mediated by Hand2. *Science*. 331(6019): 912–916.
34 Granger K, *et al.* 2024. Murine uterine gland branching is necessary for gland function in implantation. *Mol Hum Reprod*. 30(6): gaae020. https://doi.org/10.1093/molehr/gaae020
35 Nagaoka T, Inutsuka A, Begum K, Bin hafiz KM, Kishi M. 2014. Vangl2 regulates E-cadherin in epithelial cells. *Sci Rep*. 4:6940.
36 Gonzalez G, Mehra S, Wang Y, Akiyama H, Behringer RR. 2016. Sox9 overexpression in uterine epithelia induces endometrial gland hyperplasia. *Differentiation*. 92(4):204–215.
37 Hapangama DK, *et al.* 2019. Abnormally located SSEA1+/SOX9+ endometrial epithelial cells with a basalis-like phenotype in the eutopic functionalis layer may play a role in the pathogenesis of endometriosis. *Hum Reprod*. 34(1):56–68.
38 Roberts E. 2024. Loss of PRICKLE1 promotes abnormal endometrial epithelial architecture, reduced fertility, and decreased embryo implantation in mice. *Reproduction* (Epub ahead of print.). https://doi.org/10.1530/REP-24-0344.
39 Stuart T, *et al.* 2019. Comprehensive integration of single-cell data. *Cell*. 177(7):1888–1902.e21.
40 Aran D, *et al.* 2019. Reference-based analysis of lung single-cell sequencing reveals a transitional profibrotic macrophage. *Nat Immunol*. 20(2):163–172.
41 Cloud AS, *et al.* 2022. Loss of the repressor REST affects progesterone receptor function and promotes uterine leiomyoma pathogenesis. *Proc Natl Acad Sci U S A*. 119(44):e2205524119.
42 Cheong ML, Lai TH, Wu WB. 2019. Connective tissue growth factor mediates transforming growth factor beta-induced collagen expression in human endometrial stromal cells. *PLoS One*. 14(1): e0210765.
43 Zhang D, *et al.* 2016. Correlation between Cyr61 expression and clinicopathologic parameters in adenomyosis. *J Reprod Immunol*. 118:42–49.
44 Karamanou K, *et al.* 2017. Lumican effectively regulates the estrogen receptors-associated functional properties of breast cancer cells, expression of matrix effectors and epithelial-to-mesenchymal transition. *Sci Rep*. 7:45138.
45 Wang H, Li QF, Chow HY, Choi SC, Leung YC. 2020. Arginine deprivation inhibits pancreatic cancer cell migration, invasion and EMT via the down regulation of Snail, Slug, Twist, and MMP1/9. *J Physiol Biochem*. 76(1):73–83.
46 Yue X, *et al.* 2016. Leukemia inhibitory factor promotes EMT through STAT3-dependent miR-21 induction. *Oncotarget*. 7(4): 3777–3790.
47 Rutanen EM, Nyman T, Lehtovirta P, Ämmälä M, Pekonen F. 1994. Suppressed expression of insulin-like growth factor binding protein-1 mRNA in the endometrium: a molecular mechanism associating endometrial cancer with its risk factors. *Int J Cancer*. 59(3):307–312.
48 Bassuk AG, *et al.* 2008. A homozygous mutation in human PRICKLE1 causes an autosomal-recessive progressive myoclonus epilepsy-ataxia syndrome. *Am J Hum Genet*. 83(5):572–581.
49 La Manno G, *et al.* 2018. RNA velocity of single cells. *Nature*. 560(7719):494–498.
50 Ran J, *et al.* 2020. ZEB1 modulates endometrial receptivity through epithelial-mesenchymal transition in endometrial epithelial cells in vitro. *Biochem Biophys Res Commun*. 525(3):699–705.
51 Sadłecki P, Jóźwicki J, Antosik P, Walentowicz-Sadłecka M. 2020. Expression of selected epithelial-mesenchymal transition transcription factors in endometrial cancer. *Biomed Res Int*. 2020: 4584250.
52 Bartley J, Jülicher A, Hotz B, Mechsner S, Hotz H. 2014. Epithelial to mesenchymal transition (EMT) seems to be regulated differently in endometriosis and the endometrium. *Arch Gynecol Obstet*. 289(4):871–881.
53 Zhou W, Peng Z, Zhang C, Liu S, Zhang Y. 2018. ILK-induced epithelial-mesenchymal transition promotes the invasive phenotype in adenomyosis. *Biochem Biophys Res Commun*. 497(4): 950–956.
54 Ledinek Z, *et al.* 2023. The association of Wnt-signalling and EMT markers with clinical characteristics in women with endometrial cancer. *Front Oncol*. 13:1013463.
55 Gaynor LM, Colucci F. 2017. Uterine natural killer cells: functional distinctions and influence on pregnancy in humans and mice. *Front Immunol*. 8:467.
56 Díaz-Hernández I, Alecsandru D, García-Velasco JA, Domínguez F. 2021. Uterine natural killer cells: from foe to friend in reproduction. *Hum Reprod Update*. 27(4):720–746.
57 Zhang X, Wei H. 2021. Role of decidual natural killer cells in human pregnancy and related pregnancy complications. *Front Immunol*. 12:728291.
58 Ragkousi K, Gibson MC. 2014. Cell division and the maintenance of epithelial order. *J Cell Biol*. 207(2):181–188.
59 Wang J, *et al.* 2018. Polyploid superficial cells that maintain the urothelial barrier are produced via incomplete cytokinesis and endoreplication. *Cell Rep*. 25(2):464–477.e4.
60 Zhang H, *et al.* 2015. The homologous genes Vangl1 and Vangl2 are required for embryo implantation in the uterus of mice during early pregnancy. *Gene*. 555(2):140–149.
61 Cha J, *et al.* 2014. Appropriate crypt formation in the uterus for embryo homing and implantation requires Wnt5a-ROR signaling. *Cell Rep*. 8(2):382–392.
62 Vakilian M, Ghaedi K. 2021. A new hypothetical model for pancreatic development based on change in the cell division orientation. *Gene*. 785:145607.
63 Farley FW, Soriano P, Steffen LS, Dymecki SM. 2000. Widespread recombinase expression using FLPeR (flipper) mice. *Genesis*. 28(3-4):106–110.
64 Varghese BV, *et al.* 2013. Loss of the repressor REST in uterine fibroids promotes aberrant G protein-coupled receptor 10 expression and activates mammalian target of rapamycin pathway. *Proc Natl Acad Sci U S A*. 110(6):2187–2192.
65 McGinnis CS, Murrow LM, Gartner ZJ. 2019. DoubletFinder: doublet detection in single-cell RNA sequencing data using artificial nearest neighbors. *Cell Syst*. 8(4):329–337.e4.
66 Hao Y, *et al.* 2021. Integrated analysis of multimodal single-cell data. *Cell*. 184(13):3573–3587.e29.
67 Sasaki K, *et al.* 2024. Kupffer cell diversity maintains liver function in alcohol-associated liver disease. *Hepatology* (Epub ahead of print.). https://doi.org/10.1097/HEP.0000000000000918.
68 Zappia L, Oshlack A. 2018. Clustering trees: a visualization for evaluating clusterings at multiple resolutions. *Gigascience*. 7(7): giy083.
69 Heng TS, Painter MW; Immunological Genome Project Consortium. 2008. The Immunological Genome Project: networks of gene expression in immune cells. *Nat Immunol*. 9(10): 1091–1094.
70 Benayoun BA, *et al.* 2019. Remodeling of epigenome and transcriptome landscapes with aging in mice reveals widespread induction of inflammatory responses. *Genome Res*. 29(4):697–709.